Inherent structure landscape of hard spheres confined to narrow cylindrical channels

Mahdi Zarif [1,*] Raymond J. Spiteri [2] and Richard K. Bowles [3,4,†]

[1]*Department of Physical and Computational Chemistry, Shahid Beheshti University, Tehran 19839-9411, Iran*
[2]*Department of Computer Science, University of Saskatchewan, Saskatoon, Saskatchewan S7N 5C9, Canada*
[3]*Department of Chemistry, University of Saskatchewan, SK, S7N 5C9, Canada*
[4]*Centre for Quantum Topology and its Applications (quanTA), University of Saskatchewan, SK S7N 5E6, Canada*

(Received 20 August 2021; accepted 10 November 2021; published 3 December 2021)

The inherent structure landscape for a system of hard spheres confined to a hard cylindrical channel, such that spheres can only contact their first and second neighbors, is studied using an analytical model that extends previous results [Phys. Rev. Lett. **115**, 025702 (2015)] to provide a comprehensive picture of jammed packings over a range of packing densities. In the model, a packing is described as an arrangement of k helical sections, separated by defects, that have alternating helical twist directions and where all spheres satisfy local jamming constraints. The structure of each helical section is determined by a single helical twist angle, and a jammed packing is obtained by minimizing the length of the channel per particle with respect to the k helical section angles. An analysis of a small system of $N = 20$ spheres shows that the basins on the inherent structure landscape associated with these helical arrangements split into a number of distinct jammed states separated by low barriers giving rise to a degree of hierarchical organization. The model accurately predicts the geometric properties of packings generated using the Lubachevsky and Stillinger compression scheme ($N = 10^4$) and provides insight into the nature of the probability distribution of helical section lengths.

DOI: 10.1103/PhysRevE.104.064602

I. INTRODUCTION

Hard-sphere particle packings play a fundamental role in understanding a broad range of problems in material science. For example, mixtures of hard-sphere particles of different sizes give rise to a variety of stable crystal structures [1–4], and amorphous packings are used as the basis for describing the properties of liquids and glasses [5–12], as well as colloidal systems [13] and granular materials [14,15]. Sphere packing problems also appear in applications for computer science and information technology [16]. However, rigorous results for sphere packings are difficult to obtain. The most dense jammed packing of single component hard discs in two dimensions (2D) is the triangular packing, with an occupied volume fraction $\phi = \pi/\sqrt{12}$. Recently, it was shown that the face-centered-cubic (fcc) crystal, with $\phi = \pi/\sqrt{18} \approx 0.74$, is the most dense jammed packing of spheres in three dimensions (3D) [17], but results for amorphous structures are generally obtained using numerical and molecular simulation techniques.

The inherent structure landscape [6,18–20] provides a framework that connects the properties of a liquid to the properties of its mechanically stable jammed packings. Each configuration of the system is mapped to a local jammed structure, or inherent structure, by a rapid quench. All the configurations that map to the same inherent structure are then grouped together in a local basin of attraction, giving rise to a high-dimensional "landscape" of valleys (basins) separated by mountain passes that represent transition state saddle points. The thermodynamics and dynamics of the system can then be understood in terms of how the system samples different regions of this landscape and how it moves between basins. However, obtaining a comprehensive picture of the inherent structure landscape remains a significant challenge because of the difficulties associated with developing theories for amorphous particle packing.

Confining the fluid to small pores or narrow channels limits the number of contacts a particle can make, reducing the type of local structures that can be formed and simplifying the inherent structure landscape [21,22]. As a result, it is sometimes possible to obtain analytical results describing the nature of particle jamming. The 2D system of hard discs trapped between two lines, where the confinement only allows contacts up to the second nearest neighbors, has been studied extensively because its local packing environments are highly ordered, and the jammed states, from least to most dense, can be characterized in terms of defects [23,24]. The comprehensive description of the inherent landscape and the relationship to the properties of the fluid have facilitated a detailed analysis of glassy dynamics [25–30], hyperuniformity in amorphous packings [31], the statistical mechanics of granular materials [32], and the possibility of a Gardner transition in hard-particle systems [33]. Recent studies of this system have also revealed the existence of novel asymptotically crystalline states [34].

Both analytical [35–37] and simulation [38–41] studies have shown that spheres confined to quasi-one-dimensional cylindrical channels spontaneously form a variety of

*m_zarif@sbu.ac.ir
†richard.bowles@usask.ca

structures including, single, double, and staggered helices, as well as some achiral packings, depending on the diameter of the channel [42–44]. These helical structures have also been observed experimentally in molecular [45,46], colloidal [47,48], and athermal [49] systems. Most studies have focused on the formation of the most dense packing with a perfect structure, but, to develop connections between the thermodynamics and dynamics of fluids and the inherent structure landscape or to establish a statistical mechanics of athermal systems, it is necessary to understand the nature of defect and amorphous packings in these systems.

The goal of the current work is to develop a comprehensive picture of the inherent structure landscape for a system of hard spheres confined within a narrow cylindrical channel, where particle–particle contacts up to the nearest second neighbors are possible. This builds on our previous analysis [50] by removing the need to use assumptions concerning the nature of the defect states, identifying additional packing environments, and studying the distribution of packings for small systems. As a result, we find that the inherent structure landscape for this system has a degree of hierarchical organization, with basins formed from the arrangements of helical sections splitting into sub-basins, associated with distinct jammed states, separated by small barriers. We also use the model to understand features that appear in the probability distribution of helical section lengths in simulation-generated packings.

The remainder of the paper is organized as follows: Section II describes the model under study. Section III describes the geometry of perfect and defect helical packings. Section IV explores inherent structure landscape of the packing model for a small system before the model predictions are compared with the results of large system jammed states produced by simulation in Sec. V. Sections VI and VII contain our discussion and conclusions, respectively. The Appendix outlines the analytical calculation of the random probability distribution for helical section lengths.

II. MODEL

The model studied here consists of N three-dimensional hard spheres, with diameter σ, confined in a cylindrical narrow channel of length L with channel diameter H_d in the range of $1+\sqrt{3/4} < H_d/\sigma < 2$, which ensures spheres can only contact their first and second neighbors in either direction along the channel. The particle–particle and particle–wall interaction potentials are given by

$$U(r_{ij}) = \begin{cases} 0, & r_{ij} \geqslant \sigma \\ \infty, & r_{ij} < \sigma, \end{cases} \tag{1}$$

$$U_w(r_i) = \begin{cases} 0, & |r_{xy}| \leqslant |H_0/2| \\ \infty, & \text{otherwise}, \end{cases} \tag{2}$$

respectively, where $r_{ij} = |\mathbf{r_j} - \mathbf{r_i}|$ is the distance between particles, $|r_{xy}|$ is the magnitude of the position vector for a particle perpendicular to the wall where the center of the cylinder is located at $x = y = 0$, and the longitudinal direction of the channel extends in the z direction. The volume accessible to the particles centers is $V_0 = \pi L(H_0/2)^2$, where $H_0 = H_d - \sigma$, and the occupied volume is $\phi = 2N\sigma^3/(3LH_d^2)$.

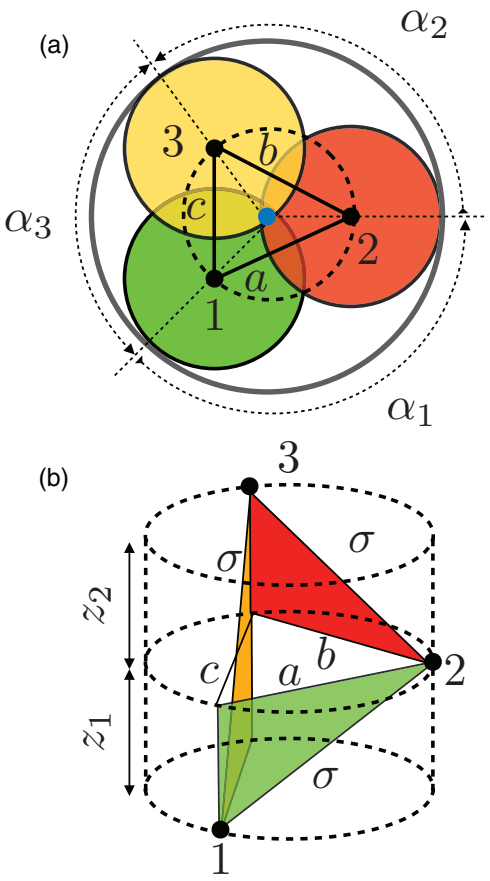

FIG. 1. Geometric construction for perfect helix. (a) The top view with black points indicating the sphere centers of particles 1, 2, 3 and the blue point marking the central axis of the cylinder. The heavy dotted line outlines the volume accessible to the particle centers and the solid gray line indicates the cylinder wall. (b) The side view showing central accessible volume. The hypotenuses of the colored triangles indicate sphere contacts with lengths σ. Spheres and external cylinder wall have been removed for clarity.

III. GEOMETRIC MODEL FOR HELICAL PACKINGS

A. Perfect helical packings

This section provides improved details of our geometric analysis presented in Ref. [50], which focused on the case of $H_d/\sigma = 1.95$. The most dense packing of the current system is a helix [44] where each sphere has four sphere-sphere contacts, formed with its first and second neighbors and a single sphere wall contact. Figure 1 shows the geometric construction used to determine the properties of the helix. Particle one is placed in the channel at a fixed point, then particle two is placed along the channel at a distance z_1 and angle α_1 in a anticlockwise direction looking from the top, such that it contacts sphere one and the wall. Particle three, which is placed at a distance z_2 and α_2 along the channel, is then constrained to contact the wall as well as particles one and two. Subsequent particles are added, alternating between increments of (z_1, α_1) and (z_2, α_2), maintaining the contact constraints until particles $N-1$ and N are forced to contact

particles one and two to ensure that the helical periodic boundary conditions are enforced.

Using this geometric construction yields the following relationships:

$$\sigma^2 = a^2 + z_1^2, \tag{3}$$

$$\sigma^2 = b^2 + z_2^2, \tag{4}$$

$$\sigma^2 = c^2 + (z_1 + z_2)^2, \tag{5}$$

$$a = H_0 \sin(\alpha_1/2), \tag{6}$$

$$b = H_0 \sin(\alpha_2/2), \tag{7}$$

$$c = H_0 \sin(\alpha_3/2), \tag{8}$$

where a, b, and c form the projected triangle connecting the particle centers. Expressions for z_1 and z_2 can be obtained by using Eqs. (6) and (7) in Eqs. (3) and (4) to give, respectively,

$$z_1^2 + \frac{H_0^2}{2}[1 - \cos\alpha_1] = \sigma^2, \tag{9}$$

and

$$z_2^2 + \frac{H_0^2}{2}[1 - \cos\alpha_2] = \sigma^2. \tag{10}$$

Substituting these results into Eq. (5) and using the constraint $\alpha_1 + \alpha_2 + \alpha_3 = 2\pi$ in Eq. (8) gives

$$\sigma^2 = \left(\sqrt{\sigma^2 - \frac{H_0^2}{2} + \frac{H_0^2}{2}\cos\left[\frac{\alpha_1}{2}\right]} + \sqrt{\sigma^2 - \frac{H_0^2}{2} + \frac{H_0^2}{2}\cos\left[\frac{\alpha_2}{2}\right]}\right)^2 - \frac{H_0^2}{2}(\cos[\alpha_1 + \alpha_2] - 1), \tag{11}$$

which can be solved numerically to provide values of α_2 as a function of α_1.

All the spheres in the helix satisfy the three-dimensional local jamming condition, where each particle has at least four contacts that are not all contained within the same hemisphere. However, this does not guarantee the system is collectively jammed because the concerted motion of particles can lead to unjamming [51]. In the limit that $H_d/\sigma \to 1 + \sqrt{3/4}$, Eq. (11) has a single solution, with $\alpha_1 = \alpha_2 = \pi$, that corresponds to the formation of the expected single zigzag chain of jammed particles. For wider channels, there is a continuous range of solutions where the variation of α_1 produces a concerted twisting motion of the helix that compresses the overall structure. To locate the most dense jammed state of the system, we then minimize the length per particle,

$$\frac{L}{N} = \frac{1}{2}(z_1 + z_2). \tag{12}$$

Figure 2 shows that L/N exhibits a single minimum as a function of α_1 in the range $1 + \sqrt{3/4} < H_d/\sigma < 1 + 4\sqrt{3}/7$, where $\alpha_1 = \alpha_2$ and $z_1 = z_2$, confirming that the most dense packings are single helices. The particle positions on the single helix can also be represented by the general helical equation,

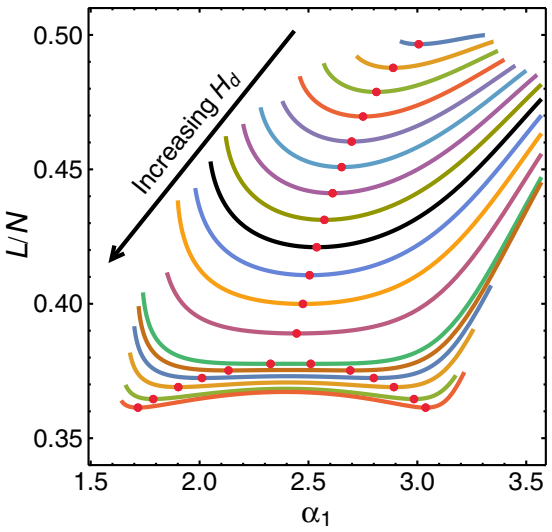

FIG. 2. Length per particle, L/N, as a function of α_1, for perfect helical sphere packings with channels diameters in the range $H_d/\sigma = 1.87$–1.999. Red points indicate local minima associated with jammed packings.

$$\{x, y, z\} = \{H_0/2\cos(n\theta + \Delta\theta),\ H_0/2\sin(n\theta + \Delta\theta),\ n\Delta z\}, \tag{13}$$

where $n = 1, 2, \ldots, N$ is an integer, $\theta = \alpha_1$ is angle of rotation between particles, $\Delta z = z_1$ is the longitudinal separation between particles, and the phase shift $\Delta\theta = 0$. Figure 3(a) shows the right-hand twist $\mathcal{P}$ helix for $H_d = 1.95$, including the line representing Eq. (13). The same packing can also be described as a symmetrical double helix, where the two chains of the helix are formed by taking every second particle, $\theta = -(2\pi - 2\alpha_1)$ to account for the change in twist direction of the double helix, $\Delta z = 2z_1$ and fixing the phase shift for the second chain as $\Delta\theta = \pi$. The double helix structure can be observed in Fig. 3(a) by following the two chains formed by the green and orange particles, respectively.

In the region $1 + 4\sqrt{3}/7 < H_d/\sigma < 2$, α_1 no longer equals α_2, and, the resulting jammed structure consists of two staggered helices [Fig. 3(b)], which leads to the appearance of two identical minima corresponding to the two possible ways of alternating between α_1 or α_2. Figure 2 also shows that for $H_d > 1 + 4\sqrt{3}/7$, the symmetrical single helix with $\alpha_1 = \alpha_2$ is located at the maximum in L/N and represents a transition state between the two possible staggered double helices.

The double-helix structure of these packings can also be described using Eq. (13) by considering chains formed by every second particle with $\theta = -[2\pi - (\alpha_1 + \alpha_2)]$ and $\Delta z = z_1 + z_2$. However, $\Delta\theta \neq \pi$ for the second chain, resulting in the staggered conformation. Mughal *et al.* [35,39] showed that the double helix could be characterized using phyllotactic indices (parastichy numbers), consisting of three positive integers, $(m + n, m, n)$, that describe the lattice structure formed by the particle centers on the surface of a cylinder of diameter H_0 (see references for full description). At the single-double helix transition point, $H_d = 1 + 4\sqrt{3}/7$, the structure is

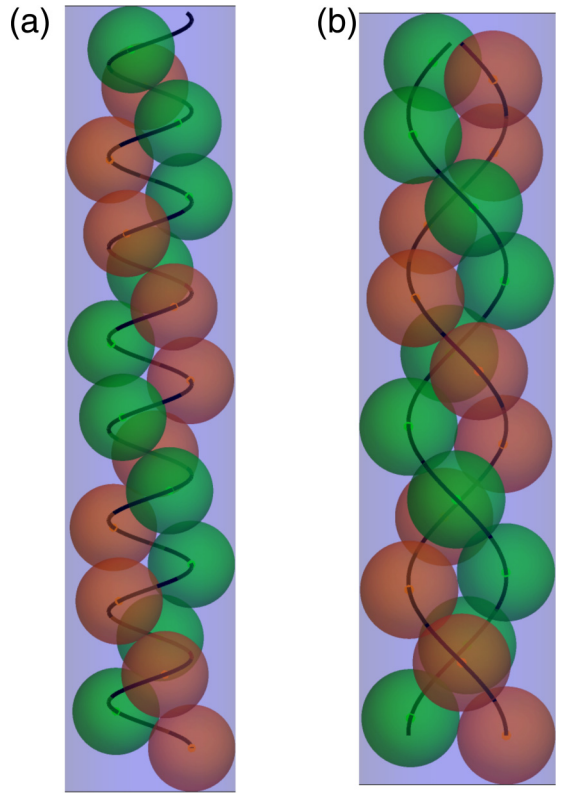

FIG. 3. Most dense packings for (a) single $\mathcal{P}$ helix with $H_d = 1.95/\sigma$ and (b) staggered double left hand twist $\mathcal{M}$ helix with $H_d = 1.995/\sigma$. Spheres have been made semitransparent, and we have introduced different colors for alternating spheres along the z axis to provide an aid to the eye. The solid black lines represent Eq. (13).

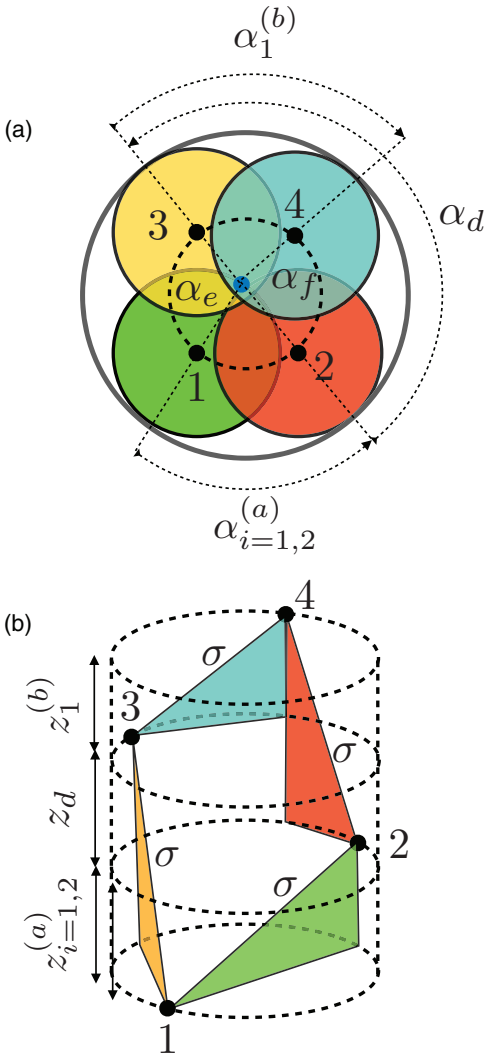

FIG. 4. Geometric construction for helical defects: (a) top view and (b) side view.

characterized as a (2,1,1) helix. As H_d increases, the symmetrical helix is deformed along every second lattice line (line-slip) to create the asymmetrical double helix until it forms the (2,2,0) structure at $H_d = 2$, which consists of alternating sphere "doublets" and is achiral [44].

The results from our geometric construction are consistent with the simulation results obtained by Pickett *et al.* [44]. It is also important to note that Fig. 2 essentially reproduces the results of Chen *et al.* [37], who used a similar approach to study the most dense perfect helical packings for $1 + \sqrt{3/4} < H_d/\sigma < 2$, and we include this figure here for completeness and to highlight the importance of the minimization of L/N with respect α_1, which plays an expanded role in determining the nature of jammed structures containing defects. Finally, it is important to note that both the right-handed ($\mathcal{P}$) and left-handed ($\mathcal{M}$) helices can be constructed by incrementing the angle in our analysis in clockwise or anticlockwise directions, respectively.

B. Defect helical packings

To generate lower density jammed states, we introduce topological defects into the helix that reverse the direction of the helical twist, noting that these must be introduced in pairs in order to maintain the helical periodic boundary conditions. As a result, a packing with k defects consists of k alternating left and right twisting sections of helix that can be characterized by a list $\{n^{(1)}, n^{(2)}, \ldots, n^{(k)}\}$, where $n^{(j)}$ specifies the number of spheres in a helical section j so that $N = \sum_{j=1}^{k} n^{(j)}$. Figure 4 shows the geometric construction used to calculate the properties of a defect located between two sections of helix, denoted with superscripts a and b, respectively. Spheres 1 and 2, which are in contact, represent the last two particles of helix section a twisting in an anticlockwise direction (from the top) and the angle α_i^a can be either α_1 ($i = 1$) if $n^{(a)}$ is even or α_2 ($i = 2$) if $n^{(a)}$ is odd. Spheres 3 and 4 are also in contact with each other and are the first two particles in helix section b, twisting in a clockwise direction. The defect is then located between particles 2 and 3 and is characterized by the longitudinal length z_d and angle α_d. To satisfy local jamming constraints, all the particles must contact the walls, sphere 3 must also contact sphere 1, and sphere 2 must contact sphere 4, but a contact between spheres 2 and 3 is not necessary.

Using the geometric construction shown in Fig. 4, we obtain the following relations for the particle separations along

the longitudinal z axis:

$$\left(z_i^{(a)}\right)^2 + \frac{H_0^2}{2}\left[1 - \cos\alpha_i^{(a)}\right] = \sigma^2, \tag{14}$$

$$\left(z_1^{(b)}\right)^2 + \frac{H_0^2}{2}\left[1 - \cos\alpha_1^{(b)}\right] = \sigma^2, \tag{15}$$

$$(z_e)^2 + \frac{H_0^2}{2}[1 - \cos\alpha_e] = \sigma^2, \tag{16}$$

$$(z_f)^2 + \frac{H_0^2}{2}[1 - \cos\alpha_f] = \sigma^2, \tag{17}$$

where α_e and α_f are the in-plane angles between particles 1 and 3, and particles 2 and 4, respectively. Substituting Eqs. (14)–(17), along with the angular constraints $\alpha_e = 2\pi - \alpha_i^{(a)} - \alpha_d$ and $\alpha_f = \alpha_d - \alpha_1^{(b)}$ into $(z_e)^2 = (z_i^{(a)} + z_d)^2$ and $(z_f)^2 = (z_1^{(b)} + z_d)^2$ yields two relations,

$$z_d^2 + \frac{H_0^2}{2}\cos\alpha_i^{(a)} + 2z_d\sqrt{\sigma^2 - \frac{H_0^2}{2}\left[1 - \cos\alpha_i^{(a)}\right]} - \frac{H_0^2}{2}\left[\cos\left(\alpha_i^{(a)} + \alpha_d\right)\right] = 0, \tag{18}$$

and

$$\frac{H_0^2}{2}[1 - \cos(\alpha_d - \alpha_f)] - \sigma^2 + \left(z_d + \sqrt{\sigma^2 - \frac{H_0^2}{2}\left[1 - \cos\alpha_1^{(b)}\right]}\right)^2 = 0, \tag{19}$$

that can be solved numerically to obtain z_d and α_d. Equations (18) and (19) highlight the fact that the geometric properties of the defect are a function of the properties of the helical sections on either side through their dependence on $\alpha_i^{(a)}$ and $\alpha_1^{(b)}$. This represents an improvement on our original analysis in Ref. [50], where it was assumed $\alpha_d = \pi$, a condition that is only true if the helices on both sides of the defect are the same, i.e., for what we referred to as helical defect crystals because they represent repeated units of identical left- and right-handed helical sections so the defects appear at regular spacings along the packing.

The length per particle of a configuration of spheres satisfying the contact conditions and containing k defects is then given by

$$\frac{L}{N} = \frac{1}{N}\sum_{j=1}^{k}\left[\left(\frac{n^{(j)} - A}{2}\right)z_1\left(\alpha_1^{(j)}\right) + \left(\frac{n^{(j)} - A}{2} - B\right)z_2\left(\alpha_1^{(j)}\right) + z_d\left(\alpha_i^{(j)}, \alpha_1^{(j+1)}\right)\right], \tag{20}$$

where $A = 0$ or 1 if $n^{(j)}$ is even or odd, respectively, $B = 1$ or 0 if $n^{(j)}$ is even or odd, respectively, and in determining z_d, $i = 1$ for even $n^{(j)}$ and $i = 2$ for odd $n^{(j)}$. Helical periodic boundaries are imposed for the first and last helical sections so that, for $j = k$, $j + 1 \equiv 1$. A jammed packing can then be obtained by minimizing L/N in Eq. (20) with respect to the set of k angles $\alpha_1^{(j)}$ that characterize each helical section and the jamming density, $\phi_J = 2N\sigma^3/(3LH_d^2)$. The helical periodic boundary conditions of the packing can be described by

$$\boldsymbol{r}_{i\gamma} = \boldsymbol{r}_i + n_\gamma\boldsymbol{\lambda}, \tag{21}$$

where $\boldsymbol{r}_{i\gamma}$ is the position of particle i in the γth unit cell, n_γ is an integer, and $\boldsymbol{\lambda}(\lambda_{|r_{xy}|}, \lambda_\theta, \lambda_z)$ is the lattice vector for the radial, angular θ, and longitudinal z components of the cylindrical coordinates, respectively. For each packing, $\lambda_z = L$, $\lambda_{|r_{xy}|} = 0$, and λ_θ can be obtained by summing over the signed angle of rotation between each atom where the sign alternates $(+1, -1)$, for each helical section to account for the direction of twist.

The number of possible helical arrangements for a given defect fraction, $\theta = k/N$, can be found by considering the number of ways we can distribute N indistinguishable spheres into k helical sections. The geometric contact restrictions of the defects require each section of helix to contain at least two spheres, leaving $N - 2k$ spheres to be placed without restrictions and yielding the number of helical section arrangements with k defects,

$$N_h(k) = \frac{2(N - k - 1)!}{(k - 1)!(N - 2k)!}, \tag{22}$$

where the factor for of two appears because we can choose to begin twisting the first helical section in either a clockwise or anticlockwise direction. Taking the natural logarithm of Eq. (22) and using Stirling's approximation then gives, in the thermodynamic limit,

$$\frac{\ln N_h(\theta)}{N} = (1 - \theta)\ln(1 - \theta) - \theta\ln\theta - (1 - 2\theta)\ln(1 - 2\theta), \tag{23}$$

where $0 \leqslant \theta \leqslant 0.5$. The total number of helical arrangements can be obtained by summing over all possible values of $k = 0, 1, \ldots, N/2$ in Eq. (22), to obtain

$$\lim_{N\to\infty}\frac{\ln N_h}{N} = \ln\left(\frac{1 + \sqrt{5}}{2}\right) \approx 0.481. \tag{24}$$

Equation (23) is the same distribution of structures found in the 2D model of hard discs confined between two lines where only nearest-neighbor contacts are allowed [23]. However, in the 2D model, θ is directly linked to the jamming density ϕ_J, which is independent of the way the defects are arranged, and there is only one jammed state associated with each defect arrangement. As we will see, this is not the case for the current model, so $N_h(\theta)$ becomes a lower bound on the number of jammed states, and ϕ_J for a packing is not only determined by θ, but it also depends on how the defects are distributed.

IV. SMALL-SYSTEM JAMMED PACKINGS

To understand how the presence of defects affects the overall structure of the packings, we begin by studying a system of $N = 50$ spheres containing just two defects and two sections of helix, denoted a and b, for a case where $H_d/\sigma = 1.95$. Figure 5(a) shows a contour plot of L/N, from Eq. (20), as a function of $\alpha_1^{(a)}$ and $\alpha_1^{(b)}$ for a system $\{n^{(a)}, n^{(b)}\} = \{15, 35\}$. When the defects are well separated and both helix sections contain an odd number of spheres, the minimum occurs where $\alpha_1^{(a)} = \alpha_1^{(b)}$, at a value where $\alpha_1 = \alpha_2$ within both sections of helix. As a result, the jammed packing consists of two sections

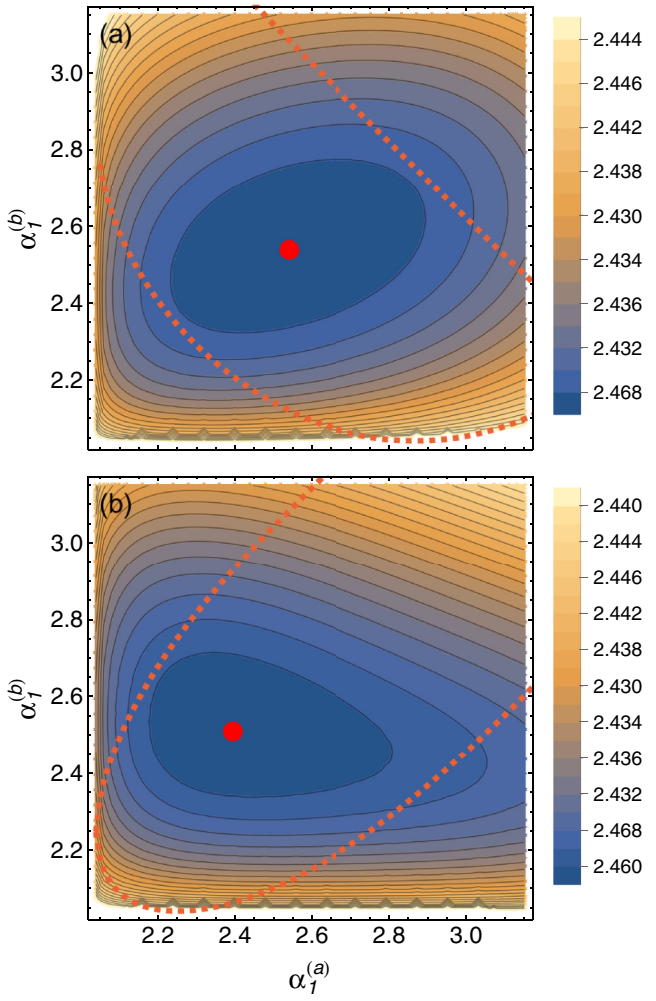

FIG. 5. Contour plots of L/N as a function of $\alpha_1^{(a)}$ and $\alpha_1^{(b)}$ for packings (a) {15, 35} and (b) {14, 36}, with $H_d/\sigma = 1.95$. Contours are separated by 0.001, the red dashed lines represent the contact constraint between particles 2 and 3 in the defects, and the red points denote the minima.

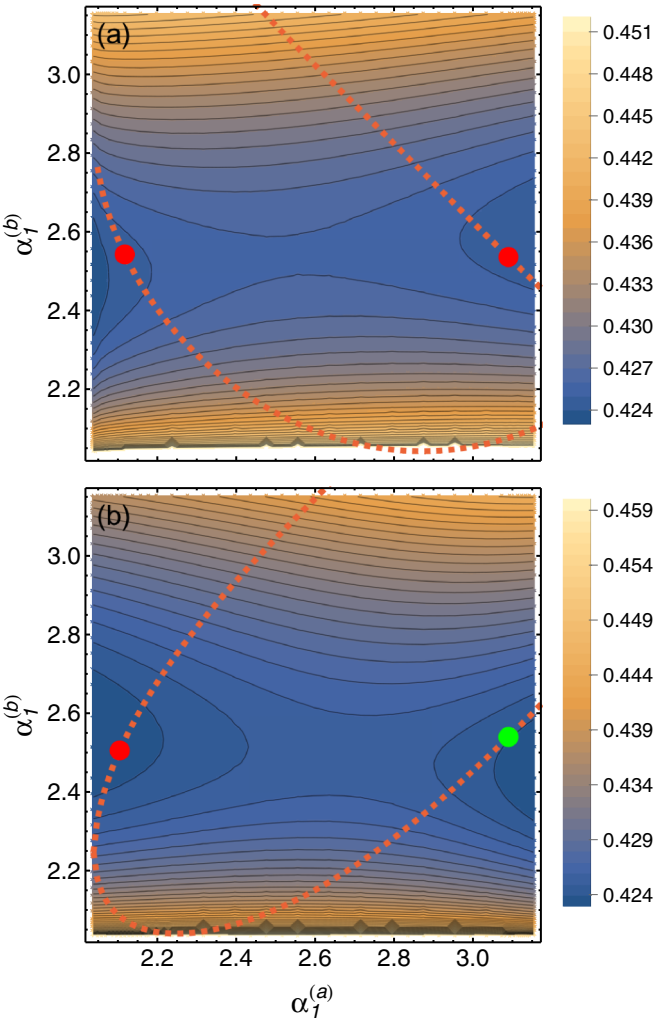

FIG. 6. Contour plots of L/N as a function of $\alpha_1^{(a)}$ and $\alpha_1^{(b)}$ for packings (a) {3,47} and (b) {2,48}, with $H_d/\sigma = 1.95$. Contours are separated by 0.001, the red dashed lines represent the contact constraint between particles 2 and 3 in the defects, and the red and green points denote a global minimum and a local minimum, respectively.

of a perfect single helix, identical to the most dense structure, with opposite $\mathcal{P}$ and $\mathcal{M}$ twists, separated by a large volume defect.

When the two helical sections contain an even number of spheres, such as $\{n^{(a)}, n^{(b)}\} = \{14, 36\}$ [see Fig. 5(b)], $\alpha_1^{(a)} \neq \alpha_1^{(b)}$, so that the two sections no longer have the same structure. Furthermore, within each section, $\alpha_1 \neq \alpha_2$, indicating the structure has changed to that of a double helix. In this case, the presence of a single defect has disrupted the entire global structure of the packing. Figure 5 also shows that, when the defects are well separated (large helical sections), the minima are located away from the contact constraint between particles 2 and 3 in the defect, indicating there is a gap between the particles.

As the defects are brought closer together, by decreasing the size of one of the helical sections, the surface of the minimum elongates along the $\alpha_1^{(a)}$ axis before eventually splitting in two when $n^{(a)} \approx 10$. Figure 6 shows that the system becomes jammed when particles 2 and 3 in the defect come into contact, locking the structure in place. Now, $\alpha_1^{(a)} \neq \alpha_1^{(b)}$ for odd-numbered helical sections, but the two minima have the same L/N and result from a switching between the values of α_1 and α_2 within a section. Nevertheless, the two packings are distinct structures because they are separated by a barrier, and it requires the concerted motion of the relative position of all the particles to move from one state to the other. The jamming densities of the two states are not the same for the even-number helical sections (Fig. 6).

Figure 7(a) shows ϕ_J, where Eq. (20) has been minimized, as a function of $n^{(a)}$ for a system containing two defects, with $H_d/\sigma = 1.95$, and we have only identified the global density maxima (L/N global minima) for each $n^{(a)}$. For $N = 100$, as $n^{(a)}$ is varied, the structure $\{n^{(a)}, N - n^{(a)}\}$ oscillates between structures where both sections of helix are odd-sized and then both sections are even-sized. The jamming density of the even-sized sections increases as $n^{(a)}$ decreases, bringing the defects closer together, whereas ϕ_J for the structures with

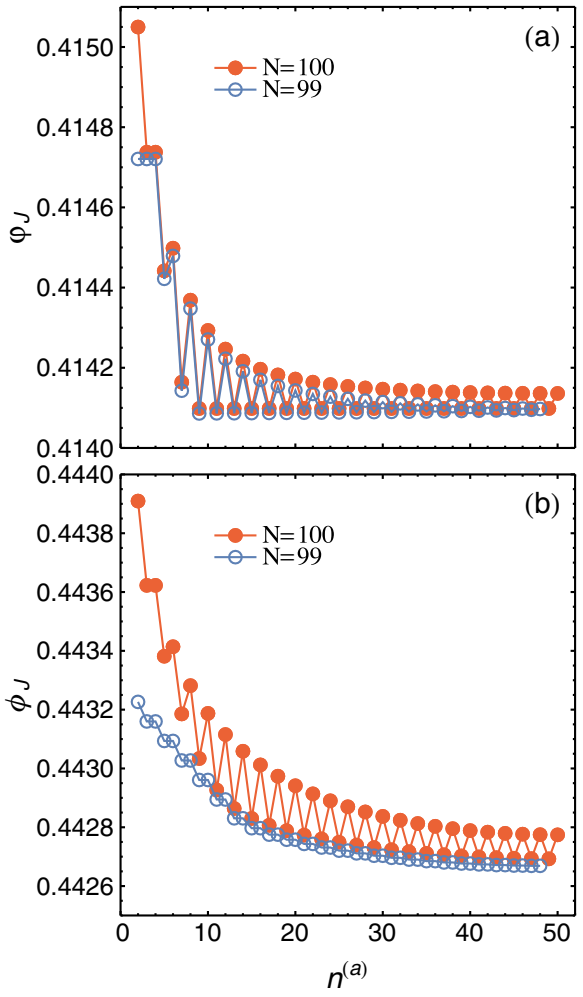

FIG. 7. The jamming occupied volume fraction, ϕ_J, for packings $\{n^{(a)}, N - n^{(a)}\}$ as a function of $n^{(a)}$ for systems with $N = 100$ (filled circles) and $N = 99$ (open circles) for (a) $H_d/\sigma = 1.95$ (b) $H_d/\sigma = 1.99$. Only the most dense structure for each $\{n^{(a)}, N - n^{(a)}\}$ is included.

odd-sized sections remains constant until $n^{(a)} < 10$. When $N = 99$, $n^{(a)}$, the smaller of the two helical sections, oscillates between odd and even, and we see a similar trend in ϕ_J, where ϕ_J is lower when $n^{(a)}$ is odd. Figure 7(b) shows the same analysis for a system with $H_d/\sigma = 1.99$, where the most dense state is a double helix. The behavior of ϕ_J for the even helical sections remains the same as observed for the narrower channel and increases as $n^{(a)}$ decreases. However, we now see ϕ_J for the odd helical sections increasing over the entire region. In addition, α_i in both odd helical sections differ from those of the perfect helix.

The analysis of a system with just two defects clearly shows that the way the defects are distributed within a packing influences ϕ_J, suggesting it is worth examining packings with an increased number of defects. The total number of jammed packings increases exponentially with N, but the simplicity of the packing model described in Sec. III means that it is possible to generate all the possible model packings for small systems and examine the full jamming landscape. The challenge of finding all the jammed structures is simplified by recognizing that all the helical arrangements, under periodic boundaries, can be generated from a series of canonical arrangements by a rotation, $\{n^{(1)}, n^{(2)}, \ldots, n^{(k)}\} \rightarrow \{n^{(k)}, n^{(1)}, \ldots, n^{(k-1)}\}$ or a reversal of the order, $\{n^{(1)}, n^{(2)}, \ldots, n^{(k)}\} \rightarrow \{n^{(k)}, n^{(k-1)}, \ldots, n^{(1)}\}$, then any replicated states can be removed. For example, the canonical arrangement $\{2, 2, 3, 2, 2, 9\}$, generates six distinct arrangements by rotation, but the operation of reversal generates six identical arrangements, which are then removed to leave the original six. However, for $\{2, 2, 2, 3, 2, 9\}$, the rotation and reversal operations generate a total of 12 distinct arrangements.

TABLE I. The number of canonical helical arrangements compared with the total number for small systems.

N	N_c	N_h
16	54	306
20	238	2091
24	1206	14330
32	38889	673135

All structures related to the same canonical arrangement maintain the same relative position of all the helical sections and minimize to a set of jammed structures with the same respective geometric properties, with the same set of $\alpha_1^{(j)}$ and jamming density. In addition, each helical arrangement actually represents two possible arrangements that can be formed by winding in the opposite direction, but the arrangements will again minimize to structures with the same geometric properties. This mechanical approach lets us count the number of states associated with each canonical arrangement and reproduces the same total number of helical arrangements as predicted by Eq. (22). Table I compares the number of canonical arrangements, N_c, with the total number of helical arrangements, N_h, for a series of small system sizes and highlights the significant reduction in the number of arrangements that need to be analyzed.

Here, we study systems of $N = 20$ spheres with $H_d/\sigma = 1.95$ and 1.99, respectively, by searching for the jammed packings associated with all of their 238 canonical helical arrangements. Since the basin for a given helical arrangement can split into sub-basins, as shown in Fig. 6, we use the local optimization, Nelder-Mead algorithm in *Mathematica* [52] and perform five minimizations of Eq. (20) for each helical arrangement with randomized initial starting points. While this does not ensure we find the global minimum for each helical arrangement, and a larger number of trials for each arrangement could reveal additional jammed states, it allows us to explore the general features affecting the appearance of sub-basins. We will also focus our analysis on arrangements that start with a single direction of twist for the first helical section because the other starting twist direction will yield the same results for ϕ_J.

To begin, it is useful to examine some of the properties of a few particular packings. The perfect helix arrangement, {20}, i.e., with $\theta = 0$, has a single canonical structure that leads to one and two jammed structures for $H_d/\sigma = 1.95$ and 1.99, respectively, as discussed earlier. The {10, 10} canonical

arrangement represents a single arrangement that minimizes to a single jammed structure, where $\alpha_1^{(j)}$ is the same for all helical sections, which is also true for {2, 2, 2, 2, 2, 2, 2, 2, 2, 2} ($\theta = 0.5$). For the {5, 5, 5, 5} arrangement, we see a more complex set of jammed states. With $H_d/\sigma = 1.95$, we find two distinct packings where $\alpha_1^{(j)}$ is the same in all four helical sections, one where the list of angles $\{\alpha_1^{(j)}\} = \{2.2943, 2.2943, 2.2943, 2.2943\}$ and the other with $\{\alpha_1^{(j)}\} = \{2.8104, 2.8104, 2.8104, 2.8104\}$. We can understand the appearance of these packings by noting the helical sections containing an odd number of spheres have an even number of alternating angles, $\alpha_1^{(j)}$ and $\alpha_2^{(j)}$ [see Eq. (20)], where the second angle is a function of the first. In the first packing, $\alpha_1^{(j)} = 2.2943$ and $\alpha_2^{(j)} = 2.8104$, so it is possible to construct the second packing by simply interchanging the two angles. For $H_d/\sigma = 1.99$, these uniform packings, where $\alpha_1^{(j)}$ is the same in all helical sections, are replaced by packings that alternate $\alpha_1^{(j)}$; i.e., $\{\alpha_1^{(j)}\} = \{1.7639, 2.7512, 1.7639, 2.7512\}$ and $\{\alpha_1^{(j)}\} = \{2.7512, 1.7639, 2.7512, 1.7639\}$. In addition, we also find that the {5, 5, 5, 5} helical arrangement, for both channel diameters, jams in a series of asymmetrical structures, where two of the helical sections are the same, but the remaining two are different; i.e., for $H_d/\sigma = 1.95$ we find $\{\alpha_1^{(j)}\} = \{2.5378, 3.0837, 2.5378, 2.1206\}$, which functions as a canonical structure for four additional jammed states. As a result, the inherent structure basin associated with the {5, 5, 5, 5} helical arrangement splits into a total of six distinct jammed states. These sets of structures illustrate the complexity of the packings that arise, despite the simplicity of the model. In particular, it is evident that while every helical section is a perfect double helix, sections within a packing can adopt double helix structures with different properties characterized by $\alpha_1^{(j)}$, even when they have the same number of particles as other sections. The diversity of helical section structures increases as we begin to study packings with different section sizes, giving rise to the "poly helical" description of the packings.

In Fig. 8, we show a number of the jammed packings for a system with $N = 20$, where the defect particles (the first and last particles in each helical section) are highlighted in a pale color, along with a plot of the angle α_i between particles i and $i + 1$. Figure 8(a) shows the {8, 12} packing, starting with a double ($\mathcal{M}$) helix that switches to a right-hand ($\mathcal{P}$) twist after the defect and that the two helical sections adopt double helix structures characterized by different angles. The two defect particles do not contact each other, but a line of contacts persists along each of the helical chains. A comparison of Figs. 8(b) and 8(c) shows how the structure can change with the movement of a defect, while the total number of helical sections remain the same. It is also worth noting that the two six-sphere helical sections in the {5, 3, 6, 6} packing are characterized by different helical twist angles because they have different overall environments. Figure 8(d) shows the least dense structure of the system, where almost all the particles are defect particles and the helical section lengths are small, causing the defect particles to touch. The variety of jammed structures results from the system needing to satisfy the global set of constraints. Our analysis also shows that Eqs. (22)–(24)

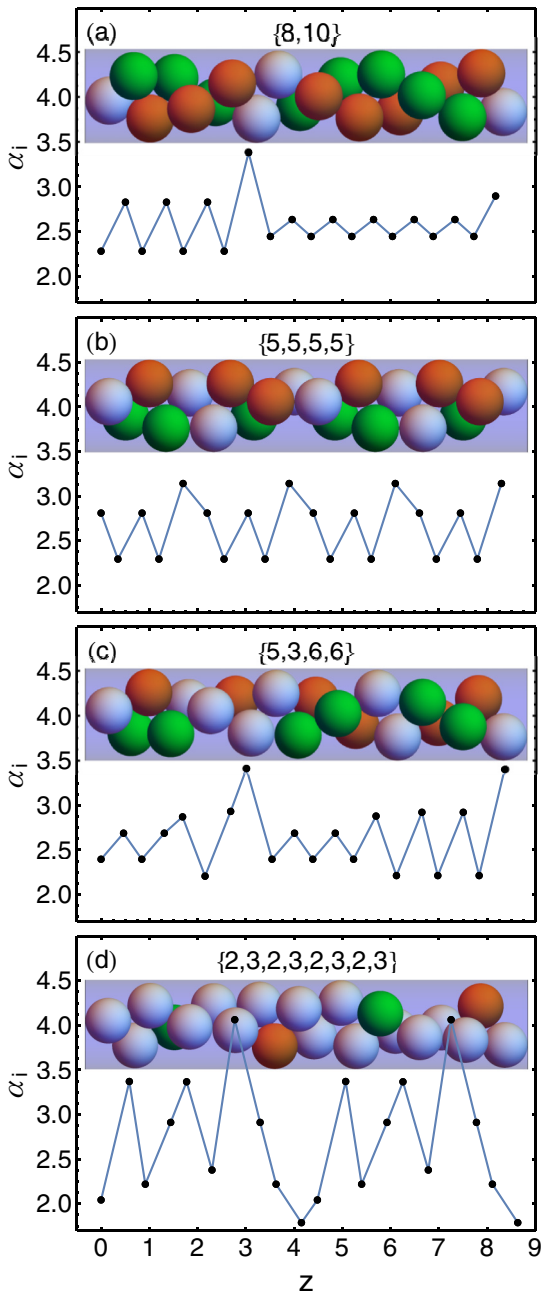

FIG. 8. α_i between particles as a function z for jammed packings ($N = 20$) (a) {8, 12}, (b) the symmetrical {5, 5, 5, 5}, (c) {5, 3, 6, 6}, and (d) {2, 3, 2, 3, 2, 3, 2, 3}. Insets show packings with defect spheres highlighted in a pale color.

provide a count of the number of basins, or metabasins, so they represent a lower bound to the number of jammed states because each arrangement of helical sections can minimize to more than one jammed structure. Most of the remaining canonical structures minimize to at least two distinct jammed states, and it is possible additional structures would be found with a more extensive search.

A number of factors affect the ϕ_J of a structure, including the number of defects and how the defects are distributed. To capture some of the more generic features of the jammed states, we plot [Fig. 9(a)] the distribution of most dense

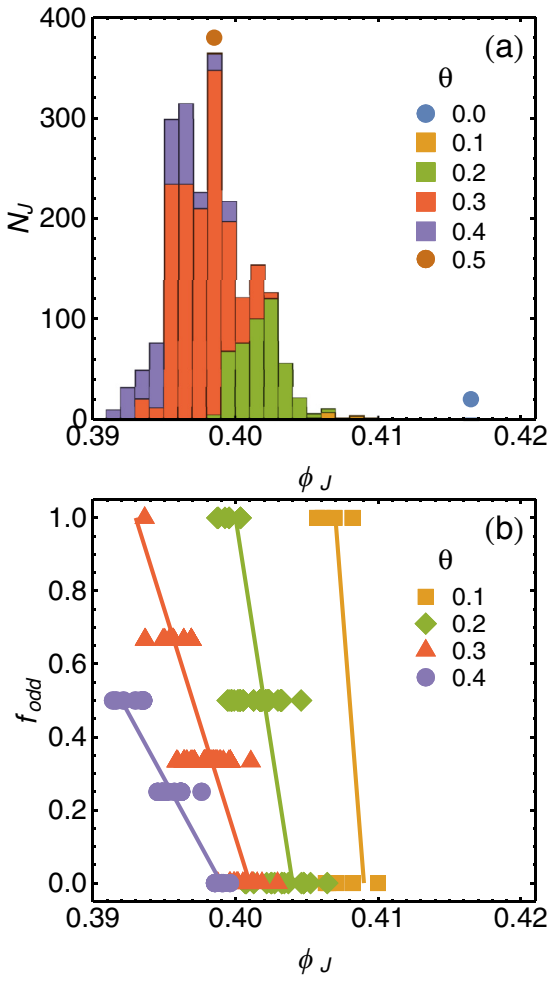

FIG. 9. (a) The cumulative number distribution of jammed states, N_J, with different θ, as a function of ϕ_J, for $H_d/\sigma = 1.95$. The ϕ_J for the jammed structure with $\theta = 0$ and $\theta = 0.5$ are highlighted with blue and brown circles, respectively. The bin size for the distribution $\Delta\phi_J = 0.001$. (b) Fraction of odd helical sections, f_{odd}, for each θ from the same distribution. Solid lines provide a guide to the eye.

jammed states obtained for each canonical structure, weighted by the number of helical arrangements it represents, which gives rise to a distribution of 2091 structures for $N = 20$, for the $H_d/\sigma = 1.95$ model. Similar results were obtained for the $H_d/\sigma = 1.99$ case [see the Supplemental Material (SM) [53]]. Each defect fraction θ exhibits a broad distribution of ϕ_J, again indicating that the jamming density is sensitive to the way the defects are organized and not just to their concentration. Notably, there is a significant gap between the ϕ_J of the most dense packing of the perfect helix and the packings with a single defect, but this is the result of the small system size and the distribution fills the density gap as N increases. Figure 9(a) also shows that the $\theta = 0.5$ jammed structure, which is the maximum defect fraction possible in the model, is not the least dense structure. Structurally, this packing is made up of two parallel zigzag chains [50]. It becomes the least dense packing in the limit $H_d/\sigma \to 1 + \sqrt{3/4}$, where the particles can only touch their first-nearest neighbors, but as $H_d/\sigma \to 2$, $\phi_J(\theta = 0.5) \to \phi_J(\theta = 0)$, and the two structures

TABLE II. Average properties of simulation generated packings, $N = 10\,000$ and $H_d/\sigma = 1.95$, using compression rate $d\sigma/dt$. The standard deviation in the last digit is given in brackets.

$d\sigma/dt$	n° packings	$\langle\phi_J\rangle$	$\langle\theta\rangle$
1×10^{-3}	65	0.4117(1)	0.044(1)
5×10^{-4}	65	0.4129(1)	0.033(1)
5×10^{-5}	153	0.4151(2)	0.011(2)

($\theta = 0.5$; $\theta = 0$) become equivalent, leading to the formation of an achiral most dense packing of alternating "doublets" [44]. However, the full distribution of jammed states is not contained between these two apparent limits, and the $\theta = 0.5$ structure moves through the distribution as the channel becomes wider.

The underlying double helix structure of the packings means that sections of helix containing odd and even numbers of spheres have different jamming properties. To examine this effect in general, we calculate the fraction of helical sections in a jammed state containing an odd number of spheres, f_{odd}, for each θ, as a function of ϕ_J. Figure 9(b) shows that increasing f_{odd} tends to decrease the jamming density, with the effect becoming greater for larger θ. This suggests that smaller sections, with odd numbers of particles, tend to pack less efficiently because they generate large defects. For the current small system studied here, the lowest density packings are formed from structures containing a mixture of helical sections with two and three particles.

V. LARGE SYSTEM SIMULATED JAMMED PACKINGS

The model developed here suggests that the jammed packings of this system adopt a "poly helical" type structure, containing a mixture of well-formed sections of single or double helix, where the properties of each helical section, such as helical pitch, depend on the distribution of the defects. To test this, we generate jammed packings by continually compressing a system of $N = 10^4$ spheres from low density, $\phi = 0.01$, using a modified version of the Lubachevsky and Stillinger (LS) molecular dynamics (MD) scheme [54], with compression rates $d\sigma/dt = 1 \times 10^{-3}$, 5×10^{-4}, and 5×10^{-5} in reduced units. Packings formed in this way have previously been shown to be jammed and follow the free volume equation of state near their jamming densities, with slower compression rates leading to increased ϕ_J, and decreased θ [50]. The average properties of the packing generated for this study are listed in Table II.

Figure 10 shows the cylindrical angle α_i between successive spheres, as a function of sphere position along the channel for a typical section of a jammed packing. Most sections have a well-defined double helix structure as denoted by the alternating values of α_1, α_2, but the values of the angles for each section differ, giving rise to the "poly helical" structure of the packing. This is consistent with our results from the study of small systems, where we find helical sections with variable $\alpha_i^{(k)}$ within one jammed packing. The configuration also shows the presence of a section of single helix containing an odd number of particles, where $\alpha_1 = \alpha_2$, as predicted

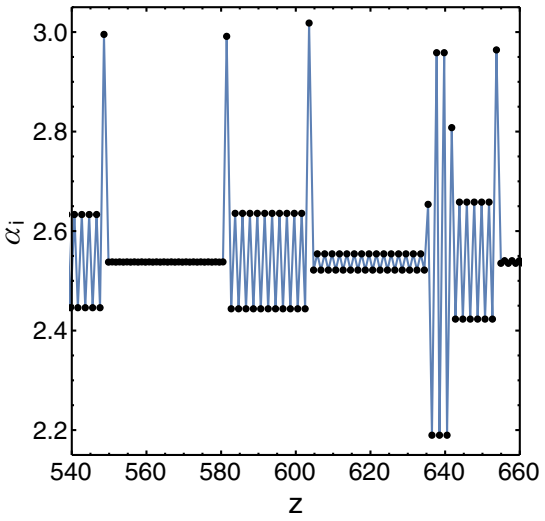

FIG. 10. The cylindrical angle between neighboring spheres, α_i, as a function of the position of the sphere along the z axis of the channel.

by the model. As a check on the validity of the packing model, we compare the geometric parameters, z_1, z_2, and α_1, obtained from the simulation, for each helical section, with the predictions of Eqs. (9)–(11). For almost all the spheres in the generated packings, we find $\Delta z_i = z_i - z_i' < 5.0 \times 10^{-6}$, where z_i $(i = 1, 2, d)$ is measured from the configurations obtained by simulation and z_i' is calculated from the model using the measured α_i. However, we do find configurations (Fig. 11) that show the presence of particles adopting spacings not predicted by the model at small values of α_1, which suggests there may be some packing environments not included in the model.

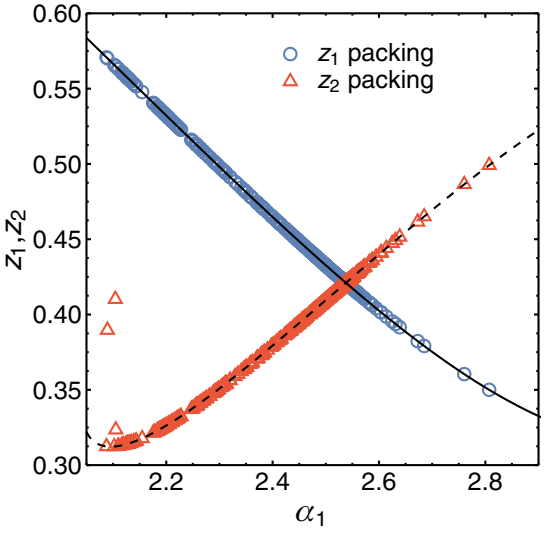

FIG. 11. Geometric properties, z_1 (circles) and z_2 (triangles), of helical sections in a jammed packing, formed using $d\sigma/dt = 0.001$ as a function of measured α_1, compared with predictions of the model (solid and dashed lines, respectively).

The packings can be further characterized in terms of the probability $P(n)$ of finding a helical section of length n, where we calculate the distribution over packings formed with the same compression rate because they have similar θ and ϕ_J. The location of the defects in the simulation-generated packings can be identified by using the local geometric properties of the particles (see SM [53] for details), which includes calculating a volume, $v_{tet}(i)$ for each particle as the volume of the tetrahedron formed by particles, $i-1$, i, $i+1$, and $i+2$. The sign of $v_{tet}(i)$ captures the local twist direction of the helix so the particles in the same helical section have the same sign, and in most cases, the sign changes at a defect. The probability distribution, $P(|v_{tet}(i)|)$ (Fig. S1), also shows the defects all have small volumes compared with those in the helical sections, providing an additional tool for locating and counting defects. To compare this to the random distribution, $P_R(n)$ (see the Appendix for details), we also calculate a nonequilibrium potential of mean force (PMF),

$$\mathrm{PMF} = -\ln \frac{P(n)}{P_R(n)}, \tag{25}$$

which will be zero if the distributions are the same and negative if helical section lengths are more probable than random. Figure 12 shows the distributions of odd and even helical sections exhibit similar properties at larger n, but at small n, the probability of finding an odd-sized helical section rapidly decreases. Notably, the probability maximum for the odd sections moves to larger section sizes with decreasing compression rate, moving from $n \approx 20$ at $d\sigma/dt = 1 \times 10^{-3}$ to $n \approx 50$ at $d\sigma/dt = 5 \times 10^{-5}$. We also see the presence of sections with $n = 1$ that are not predicted by the model, although only with a low probability. At the fastest compression rate $P(n)$ for the even-sized sections decreases monotonically with increasing n, with the exception of the $n = 2$ section, but as $d\sigma/dt$ decreases, the distribution develops a shoulder and then becomes bimodal at the slowest compression rate. As a result, the PMF exhibits two minima, one at small n and another at larger n, separated by a barrier.

VI. DISCUSSION

The inherent structure paradigm applied to hard particle systems describes the statistical mechanics of the fluid by grouping together all the configurations that map the same jammed state into a local basin of attraction. The thermodynamics and dynamics of the fluid and glassy behavior can then be described in terms of the properties of the accessible basins and how the system moves between them. The goal of the current work is to develop an accurate model of the jammed states for this quasi-one-dimensional model, in terms of helical structures, that improves on the defect crystal model developed previously. In particular, the new model now includes odd-sized helical sections and does not assume a regular arrangement of the defects, which helps account for a broader range of helical arrangements. The model does miss some possible arrangements, such as the presence of neighboring defects observed in simulation, but this state appears to be rare and further decreases in probability as the compression rate is decreased. Furthermore, our approach to generating the distribution of jammed packing can be viewed as introducing

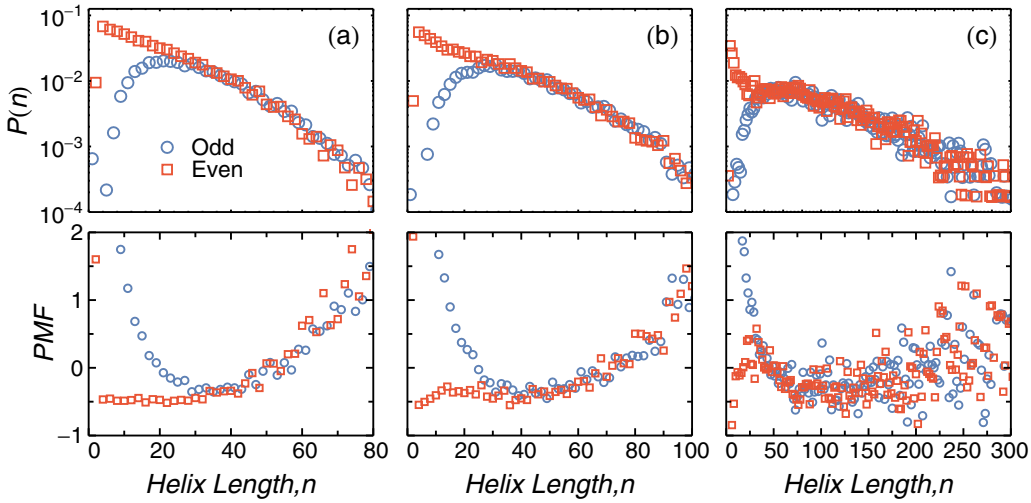

FIG. 12. (top row) Probability $P(n)$ of finding a helix section containing n spheres for jammed packing with $H_d = 1.95$ and $N = 10\,000$. Formed with (a) $d\sigma/dt = 1 \times 10^{-3}$, (b) $d\sigma/dt = 5 \times 10^{-4}$, and (c) $d\sigma/dt = 5 \times 10^{-5}$. (bottom row) Corresponding potential of mean force.

defects as a perturbation on the structure of the perfect most dense helical structure for a given channel diameter. If other perfect helical structures exist that are not related to the most dense packing through a combination of the defects described in our model, then it may be possible to generate additional defects structures not included here. Nevertheless, our current model accurately reproduces the helical geometries found in large packings generated by the LS simulation.

The model for jammed packings also reveals that the inherent structure landscape has some degree of hierarchical organization, where the basins of configuration space associated with a given arrangement of helical sections split into sub-basins for distinct jammed states. A single helical arrangement represents a basin on the inherent structure landscape because, at high density, there is a significant barrier to moving a particle from one section of helix, which is twisting in one sense, to the next helical section, which is twisting in the opposite sense. For example, particles 3 and 4 in Fig. 4 would need to swap places in terms of the anticlockwise rotation so that the defect becomes located between particles 3 and 4, and particle 3 moves from one helical section to another. Figure 6 then shows these basins can split further into smaller sub-basins, each associated with distinct jammed states that are separated by a small barrier. As the number of helical sections increases, we see an increasingly complex set of minima located within the basin of a given helical arrangement.

A highly successful mean-field theory [55] of the bulk hard-sphere glass transition in high dimensions also predicts the presence of a Gardner transition [56] between stable and marginally stable glasses that is associated with the repeated fracturing of inherent structure basins into sub-basins at high densities. There is growing evidence to suggest the Gardner transition persists down to three dimensions [57,58], making it relevant to real glassy materials. However, it has also been argued that the physics observed in these lower dimensions results from an avoided transition [33]. The quasi-one-dimensional nature of our system suggests that it is unlikely to exhibit a Gardner transition and the types of particle rearrangements involved in the transition between sub-basins are globally concerted motions rather than the highly localized motion thought to be important in bulk glasses. For example, Fig. 6 shows that the angle characterizing the structure changes in both helical sections, even though the change in the longer helical section is small and within the $\{5, 5, 5, 5\}$ helical arrangement, the transition from the jammed packing, $\{\alpha_1^j\} = \{2.2943, 2.2943, 2.2943, 2.2943\} \rightarrow \{2.8104, 2.8104, 2.8104, 2.8104\}$, requires significant changes in all helical sections. However, the properties of the sub-basins still need to be studied in larger systems. The connectivity of the sub-basins also remains to be explored because it is not clear whether the sub-basins show repeated hierarchical organization as expected in bulk glasses. Nevertheless, access to a detailed model of the inherent structure landscape for this system opens up the possibility of understanding how the presence and organization of sub-basins influence the properties of materials at high density.

Our study of jammed packings in small systems shows that ϕ_J depends on more than the defect fraction. Figure 7 shows that, in the case of a system with two defects, the number parity of the system influences ϕ_J. The effect arises because of the asymmetric nature of the double helix formed in the presence of the defects. The odd- and even-sized sections have different numbers of angular increments, α_1 and α_2, and $\alpha_1 \neq \alpha_2$, resulting in different packing effects. However, with increasing helical section size, the two angles approach those of the perfect structure, and we see a decrease in the parity effects.

The presence of small odd-sized packings tends to lower the packing density due to a large defect length. Figure 9 shows that ϕ_J varies over a large range for any given θ and that increasing the fraction of odd sections leads to lower densities, with the least dense packing consisting of alternating sections of two and three particles. Similarly, Fig. 7 shows that small, odd-sized helical sections lead to a decrease in ϕ_J relative to similar sized, even-sized sections. This inefficiency of packing

for small, odd-sized sections has a significant effect on the distribution of helical sections lengths of the large system packing formed in simulation. The LS molecular dynamics scheme continually expands the particles during the trajectory, allowing the system to relax during compression and move to denser basins on the inherent structure landscape that have greater vibrational entropy until the fluid eventually falls out of equilibrium and finally becomes jammed. Figure 12 shows that the smaller, odd-sized, helical sections are preferentially eliminated from $P(n)$ due to their inefficient packing, leading to a nonmonotonic distribution with a maximum. As the compression rate decreases, the fluid samples denser basins on the inherent structure landscape by continuing to eliminate the least efficient packing elements, which moves the maximum in the odd-sized helical section to larger sizes. However, it is not clear how far this process goes with further decreases in compression rate because the odd and even helical sections become more similar with increasing n.

Earlier [50], it was shown, using a defect crystal model, that this system exhibits a long-range defect-defect attraction that results from an increase in ϕ_J, and hence the vibrational entropy, as two defects approach. Figure 7 shows that the same picture persists for a single pair of defects with the improved model, although the inclusion of the odd-sized helical sections complicates the details by adding an oscillation to the attraction. Furthermore, Fig. 12 clearly shows the PMF for the even-sized sections develops two minima at slow compression rates, one at small n and a second one at larger separations, suggesting the defect-defect attraction leads to a degree of defect pairing. One-dimensional and quasi-one-dimensional systems with particles interacting via short-ranged potentials cannot exhibit a phase transition because there is an entropic advantage in the thermodynamic limit associated with introducing defects that breaks up long-range order [59–61]. However, if the interactions between defects become sufficiently long-ranged, phase transitions can occur [62,63]. Hu *et al.* [64] recently obtained numerically exact results using the transfer matrix method that shows that a transition does not occur in this system, suggesting the configurational entropy, which is related to the number of defects, still dominates at high density, despite the defect-defect attraction driven by the vibrational entropy. The fact that the PMF for the odd-sized helical sections only exhibits a single minimum at large n, and that the PMF for the even-sized sections has a large barrier at $n = 2$, reducing defect-defect annihilation, may work to counter the attractive interaction and help prevent a transition. Finally, we also note that $P(n)$, and hence the PMF, are obtained from a nonequilibrium compression of the fluid. It is likely that the jammed states retain some properties of the equilibrium fluid when they fall out of equilibrium, but kinetic effects, such as defect creation and annihilation mechanisms and the ability of defects to diffuse through the structure, could play a role in determining the properties of the packings.

VII. CONCLUSIONS

A model for the jammed packings of hard spheres confined to a narrow cylindrical channel, allowing only next-nearest contacts, has been developed. It assumes all particles satisfy local packing constraints and describes the structure in terms of helical sections, with alternating twist direction, separated by defects. While it is possible that additional local packing environments could be found, the model provides an improved description of the defects in the packings, as well as packings with odd-sized helical sections, compared with the defect crystal model developed earlier, and accurately reproduces the geometries of jammed packings created by molecular dynamics simulation. The model also confirms the possibility of an entropically driven defect-defect attraction that appears to influence the structure of the particle packings.

ACKNOWLEDGMENTS

We would like to acknowledge National Sciences and Engineering Research Council of Canada (NSERC) grants RGPIN–2019–03970 (R.K.B) and RGPIN-2020-04467 (R.J.S.) for financial support. Computational resources were provided by the ICT at the University of Saskatchewan, WestGrid, and Compute Canada.

APPENDIX: RANDOM DISTRIBUTION OF HELICAL SECTION LENGTHS

Here, we derive the random distribution of helical section lengths to obtain an expression for the probability $P_R(n)$ of finding a helical section of length n in a system of N spheres containing k defects. It is more convenient to develop the analysis in terms of the clusters of the "bonds" connecting the neighboring spheres in contact, so that a cluster of l bonds represents a helical section of $n = l + 1$ spheres. If n_0 is the total number of nondefect bonds and q_l is the number of clusters of with l bonds, then we have the following constraints:

$$n_0 = \sum_{l=1}^{\infty} l q_l = N - k, \tag{A1}$$

and

$$k = \sum_{l=1}^{\infty} q_l, \tag{A2}$$

where the conservation condition, $N = n_0 + k$, was used in the right-hand side of Eq. (A1), and Eq. (A2) arises from the requirements that each cluster be separated by a defect and defects cannot be adjacent to each other.

The random equilibrium distribution of clusters is obtained by finding the cluster distribution $\{q_l\}$ that maximizes the entropy $S/k_B = \ln \Omega$, subject to the constraints, Eq. (A1) and Eq. (A2), where

$$\Omega = \sum_{\{q_l\}} g, \tag{A3}$$

and g is the number of distinct ways to distribute the clusters. To obtain an expression for g, it is useful to begin by treating all clusters as distinguishable and then remove the over-counting of any indistinguishable clusters [65]. In a system with periodic boundaries, such that particle N contacts particle 1, there are N places to put the first cluster and $(k-1)!$ ways to place the remaining $k-1$ distinguishable clusters. The distinguishability is then removed by dividing

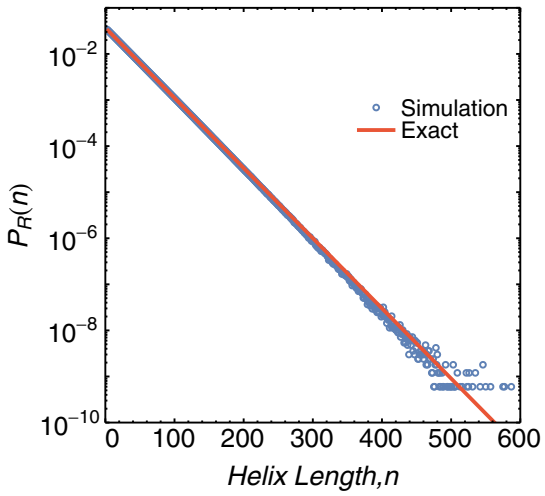

FIG. 13. Probability, $P_R(n)$, of finding a helical section containing n spheres in a random distribution of defects with $\theta = 0.0333$, from simulation (open circles) and exact theory (solid line) given by Eq. (A10).

by $q_l!$ for each l, yielding,

$$g = \frac{N(k-1)!}{\prod_{l=1}^{\infty} q_l!}. \tag{A4}$$

The maximum can be obtained by introducing the undetermined multipliers, λ_1 and λ_2, for the two constraints and setting the derivative with respect to q_m to zero, for each m,

$$\frac{\partial}{\partial q_m}\left[\ln[\{q_l\}] + \lambda_1\left(N - k - \sum_{l=1}^{\infty} l q_l\right) + \lambda_2\left(k - \sum_{l=1}^{\infty} q_l\right)\right] = 0. \tag{A5}$$

The only terms to survive are those where $m = l$, which gives

$$q_l = e^{-\lambda_1 l} e^{-\lambda_2} = S_1^l S_2, \tag{A6}$$

then using Eq. (A6) in the constraints, Eqs. (A1) and (A2), and solving for the unknowns yields

$$S_1 = \frac{N-2k}{N-k}, \tag{A7}$$

and

$$S_2 = \frac{k^2}{N-2k}. \tag{A8}$$

Using Eqs. (A7) and (A8) in Eq. (A6) and introducing the fraction of defects, $\theta = k/N$ then gives

$$\frac{q_l}{N} = \frac{\theta^2}{1-2\theta}\left[\frac{1-2\theta}{1-\theta}\right]^l. \tag{A9}$$

Finally, to be consistent with our analysis in the main text, we normalize $P_R(n)$ with respect to the number of defects rather than N and note $n = l + 1$, which gives,

$$P_R(n) = \frac{1}{\theta}\frac{q_{n-1}}{N} = \frac{\theta}{1-2\theta}\left[\frac{1-2\theta}{1-\theta}\right]^{n-1}. \tag{A10}$$

Figure 13 compares the exact result for $P_R(n)$ [Eq. (A10)], which is valid in the thermodynamic limit ($N \to \infty$), with the results obtained from simulations for a system with $N = 10\,000$, where 5×10^6 configurations were generated with randomly placed defect bonds such that there were no neighboring defects bonds and $\theta = 0.0333$. The finite-sized system accurately reproduces the exact results for the small helical sections but begins to systematically underestimate $P_R(n)$ for larger sections.

[1] J. K. Kummerfeld, T. S. Hudson, and P. Harrowell, The densest packing of AB binary hard-sphere homogeneous compounds across all size ratios, J. Phys. Chem. B **112**, 10773 (2008).

[2] A. B. Hopkins, F. H. Stillinger, and S. Torquato, Densest binary sphere packings, Phys. Rev. E **85**, 021130 (2012).

[3] L. Filion and M. Dijkstra, Prediction of binary hard-sphere crystal structures, Phys. Rev. E **79**, 046714 (2009).

[4] R. Koshoji, M. Kawamura, M. Fukuda, and T. Ozaki, Diverse densest binary sphere packings and phase diagram, Phys. Rev. E **103**, 023307 (2021).

[5] J. D. Bernal and J. Mason, Packing of spheres: Co-ordination of randomly packed spheres, Nature (London) **188**, 910 (1960).

[6] F. H. Stillinger, E. A. DiMarzio, and R. L. Kornegay, Systematic approach to explanation of the rigid disk phase transition, J. Chem. Phys. **40**, 1564 (1964).

[7] R. J. Speedy, The hard sphere glass transition, Mol. Phys. **95**, 169 (2009).

[8] A. J. Liu and S. R. Nagel, Jamming is not just cool any more, Nature (London) **396**, 21 (1998).

[9] S. Torquato, T. M. Truskett, and P. G. Debenedetti, Is Random Close Packing of Spheres Well Defined? Phys. Rev. Lett. **84**, 2064 (2000).

[10] G. Parisi and F. Zamponi, Mean-field theory of hard sphere glasses and jamming, Rev. Mod. Phys. **82**, 789 (2010).

[11] S. Torquato and F. H. Stillinger, Jammed hard-particle packings: From Kepler to Bernal and beyond, Rev. Mod. Phys. **82**, 2633 (2010).

[12] S. Torquato, Perspective: Basic understanding of condensed phases of matter via packing models, J. Chem. Phys. **149**, 020901 (2018).

[13] P. N. Pusey and W. v. Megen, Phase behaviour of concentrated suspensions of nearly hard colloidal spheres, Nature (London) **320**, 340 (1986).

[14] S. Edwards and R. Oakeshott, Theory of powders, Physica A (Amsterdam, Neth.) **157**, 1080 (1989).

[15] D. Bi, S. Henkes, K. E. Daniels, and B. Chakraborty, The statistical physics of athermal materials, Annu. Rev. Condens. Matter Phys. **6**, 63 (2015).

[16] M. Mezard and A. Montanari, *Information, Physics, and Computation* (Oxford University Press, Inc., 2009).

[17] T. Hales, A proof of the Kepler conjecture, Ann. Math. **162**, 1065 (2005).

[18] F. H. Stillinger and T. A. Weber, Hidden structure in liquids, Phys. Rev. A **25**, 978 (1982).

[19] A. Heuer, Exploring the potential energy landscape of glass-forming systems: From inherent structures via metabasins to macroscopic transport, J. Phys.: Condens. Matter **20**, 373101 (2008).
[20] M. Ozawa, T. Kuroiwa, A. Ikeda, and K. Miyazaki, Jamming Transition and Inherent Structures of Hard Spheres and Disks, Phys. Rev. Lett. **109**, 205701 (2012).
[21] R. K. Bowles and R. J. Speedy, Five discs in a box, Physica A (Amsterdam, Neth.) **262**, 76 (1999).
[22] E. R. Weeks and K. Criddle, Visualizing free-energy landscapes for four hard disks, Phys. Rev. E **102**, 062153 (2020).
[23] R. K. Bowles and I. Saika-Voivod, Landscapes, dynamic heterogeneity, and kinetic facilitation in a simple off-lattice model, Phys. Rev. E **73**, 011503 (2006).
[24] S. S. Ashwin and R. K. Bowles, Complete Jamming Landscape of Confined Hard Discs, Phys. Rev. Lett. **102**, 235701 (2009).
[25] M. Z. Yamchi, S. S. Ashwin, and R. K. Bowles, Fragile-Strong Fluid Crossover and Universal Relaxation Times in a Confined Hard-Disk Fluid, Phys. Rev. Lett. **109**, 225701 (2012).
[26] S. S. Ashwin, M. Zaeifi Yamchi, and R. K. Bowles, Inherent Structure Landscape Connection between Liquids, Granular Materials, and the Jamming Phase Diagram, Phys. Rev. Lett. **110**, 145701 (2013).
[27] M. J. Godfrey and M. A. Moore, Static and dynamical properties of a hard-disk fluid confined to a narrow channel, Phys. Rev. E **89**, 032111 (2014).
[28] M. J. Godfrey and M. A. Moore, Understanding the ideal glass transition: Lessons from an equilibrium study of hard disks in a channel, Phys. Rev. E **91**, 022120 (2015).
[29] M. Z. Yamchi, S. S. Ashwin, and R. K. Bowles, Inherent structures, fragility, and jamming: Insights from quasi-one-dimensional hard disks, Phys. Rev. E **91**, 022301 (2015).
[30] J. F. Robinson, M. J. Godfrey, and M. A. Moore, Glasslike behavior of a hard-disk fluid confined to a narrow channel, Phys. Rev. E **93**, 032101 (2016).
[31] M. J. Godfrey and M. A. Moore, Absence of Hyperuniformity in Amorphous Hard-Sphere Packings of Nonvanishing Complexity, Phys. Rev. Lett. **121**, 075503 (2018).
[32] R. K. Bowles and S. S. Ashwin, Edwards entropy and compactivity in a model of granular matter, Phys. Rev. E **83**, 031302 (2011).
[33] C. L. Hicks, M. J. Wheatley, M. J. Godfrey, and M. A. Moore, Gardner Transition in Physical Dimensions, Phys. Rev. Lett. **120**, 225501 (2018).
[34] Y. Zhang, M. J. Godfrey, and M. A. Moore, Marginally jammed states of hard disks in a one-dimensional channel, Phys. Rev. E **102**, 042614 (2020).
[35] A. Mughal, H. K. Chan, and D. Weaire, Phyllotactic Description of Hard Sphere Packing in Cylindrical Channels, Phys. Rev. Lett. **106**, 115704 (2011).
[36] A. Mughal and D. Weaire, Theory of cylindrical dense packings of disks, Phys. Rev. E **89**, 042307 (2014).
[37] H.-K. Chan, Y. Wang, and H. Han, Densest helical structures of hard spheres in narrow confinement: An analytic derivation, AIP Adv. **9**, 125118 (2019).
[38] M. C. Gordillo, B. Martínez-Haya, and J. M. Romero-Enrique, Freezing of hard spheres confined in narrow cylindrical pores, J. Chem. Phys. **125**, 144702 (2006).
[39] A. Mughal, H. K. Chan, D. Weaire, and S. Hutzler, Dense packings of spheres in cylinders: Simulations, Phys. Rev. E **85**, 051305 (2012).
[40] F. J. Durán-Olivencia and M. C. Gordillo, Ordering of hard spheres inside hard cylindrical pores, Phys. Rev. E **79**, 061111 (2009).
[41] L. Fu, W. Steinhardt, H. Zhao, J. E. Socolar, and P. Charbonneau, Hard sphere packings within cylinders, Soft Matter **12**, 2505 (2016).
[42] R. O. Erickson, Tubular packing of spheres in biological fine structure, Science **181**, 705 (1973).
[43] W. F. Harris and R. O. Erickson, Tubular arrays of spheres: Geometry, continuous and discontinuous contraction, and the role of moving dislocations, J. Theor. Biol. **83**, 215 (1980).
[44] G. T. Pickett, M. Gross, and H. Okuyama, Spontaneous Chirality in Simple Systems, Phys. Rev. Lett. **85**, 3652 (2000).
[45] W. Mickelson, S. Aloni, W.-Q. Han, J. Cumings, and A. Zettl, Packing C_{60} in boron nitride nanotubes, Science **300**, 467 (2003).
[46] A. N. Khlobystov, D. A. Britz, A. Ardavan, and G. A. D. Briggs, Observation of Ordered Phases of Fullerenes in Carbon Nanotubes, Phys. Rev. Lett. **92**, 245507 (2004).
[47] L. Jiang, J. W. J. de Folter, J. Huang, A. P. Philipse, W. K. Kegel, and A. V. Petukhov, Helical colloidal sphere structures through thermo-reversible co-assembly with molecular microtubes, Angew. Chem., Int. Ed. **52**, 3364 (2013).
[48] L. Fu, C. Bian, W. C. Shields, D. F. Cruz, G. P. López, and P. Charbonneau, Assembly of hard spheres in a cylinder: A computational and experimental study, Soft Matter **13**, 3296 (2017).
[49] A. Meagher, F. García-Moreno, J. Banhart, A. Mughal, and S. Hutzler, An experimental study of columnar crystals using monodisperse microbubbles, Colloids Surf. A **473**, 55 (2015).
[50] M. Z. Yamchi and R. K. Bowles, Helical Defect Packings in a Quasi-One-Dimensional System of Cylindrically Confined Hard Spheres, Phys. Rev. Lett. **115**, 025702 (2015).
[51] S. Torquato and F. H. Stillinger, Multiplicity of generation, selection, and classification procedures for jammed hard-particle packings, J. Phys. Chem. B **105**, 11849 (2001).
[52] Wolfram Research Inc, Mathematica 12.2 (2020).
[53] See Supplemental Material at http://link.aps.org/supplemental/10.1103/PhysRevE.104.064602 for Inherent Structure Landscape of Hard Spheres Confined to Narrow Cylindrical Channels.
[54] B. D. Lubachevsky and F. H. Stillinger, Geometric properties of random disk packings, J. Stat. Phys. **60**, 561 (1990).
[55] J. Kurchan, G. Parisi, and F. Zamponi, Exact theory of dense amorphous hard spheres in high dimension I. The free energy, J. Stat. Mech.: Theory Exp. (2012) P10012.
[56] J. Kurchan, G. Parisi, P. Urbani, and F. Zamponi, Exact theory of dense amorphous hard spheres in high dimension. II. The high density regime and the gardner transition, J. Phys. Chem. B **117**, 12979 (2013).
[57] P. Charbonneau, J. Kurchan, G. Parisi, P. Urbani, and F. Zamponi, Fractal free energy landscapes in structural glasses, Nat. Commun. **5**, 3725 (2014).
[58] L. Berthier, G. Biroli, P. Charbonneau, E. I. Corwin, S. Franz, and F. Zamponi, Gardner physics in amorphous solids and beyond, J. Chem. Phys. **151**, 010901 (2019).

[59] L. v. Hove, Sur l'intégrale de configuration pour les systèmes de particules à une dimension, Physica **16**, 137 (1950).
[60] E. Lieb and D. Mattis, *Mathematical Physics in One Dimension* (Academic Press, New York, 1966).
[61] L. Landau and E. Lifshitz, *Statistical Physics, Part 1. Course of Theoretical Physics Volume 5* (Pergamon Press, Oxford, New York, 1980).
[62] D. J. Thouless, Long-range order in one-dimensional Ising systems, Phys. Rev. **187**, 732 (1969).
[63] J. M. Kosterlitz and D. J. Thouless, Early work on defect driven phase transitions, Int. J. Mod. Phys. B **30**, 1630018 (2016).
[64] Y. Hu, L. Fu, and P. Charbonneau, Correlation lengths in quasi-one-dimensional systems via transfer matrices, Mol. Phys. **116**, 3345 (2018).
[65] M. B. Yilmaz and F. M. Zimmermann, Exact cluster size distribution in the one-dimensional Ising model, Phys. Rev. E **71**, 026127 (2005).